PCCP

Accepted Manuscript

ROYAL SOCIETY OF CHEMISTRY

www.rsc.org/pccp

Physical Chemistry Chemical Physics
CREATED USING THE RSC LaTeX PCCP ARTICLE TEMPLATE – SEE www.rsc.org/electronicfiles FOR DETAILS

PAPER

Properties and photochemistry of valence-induced-Ti^{3+} enriched (Nb,N)-codoped anatase TiO_2 semiconductors

Andrea Folli,*[ab] Jonathan Z. Bloh,[b] Anaïs Lecaplain,[b] Rebecca Walker,[b] and Donald E. Macphee[b]

Received Xth XXXXXXXXXX 20XX, Accepted Xth XXXXXXXXX 20XX
First published on the web Xth XXXXXXXXXX 200X
DOI: 10.1039/b000000x

Nb and N codoped TiO_2s are outstandingly versatile semiconductor oxides. Their high conductivity makes them valid alternatives to commercially available, but very expensive, conductive oxides. They show increased photonic efficiencies compared to the cases of solely Nb or N doped TiO_2, when used as visible light sensitised photocatalysts. Furthermore, they are excellent materials for O_2 sensors at very low temperature. Despite these remarkable properties, a clear picture of the electronic and optical mechanisms induced by the simultaneous presence of the dopants has just begun to be understood. Using a combination of electron paramagnetic resonance (EPR) spectroscopy, electrochemical impedance spectroscopy (EIS) and optical spectroscopy, we present here novel fundamental insights into the mechanisms responsible for the enhanced conductivity and visible light photochemistry.

Nb^{5+} can isomorphically and aliovalently replace Ti^{4+} in the TiO_2 crystal lattice. The difference in the valency of Nb^{5+} and Ti^{4+} not only leads to a change in the stoichiometry of the composite, it significantly influences its electrical conductivity too[1]. Very recently, the enhanced conductivity (and high refractive index) of Nb doped anatase TiO_2 was shown to be largely exploitable in fields such as: transparent conductive oxides (TCOs)[2–4], transparent electrodes for solar cells and GaN-based LEDs[5,6]. This increased conductivity seems to be associated with the formation of Ti^{3+}. Biedrzycki et al.[7] showed that Ti^{3+} centres formed as a result of valence induction when Nb^{5+} aliovalently replaces Ti^{4+} are structurally very different from the Ti^{3+} centres formed as a consequence of chemical or chemo/thermal reduction of pure TiO_2. The former seem to be delocalised bulk species with optical absorption deep in the infra-red[7] and responsible for the increased conductivity in Nb-doped TiO_2 (effectively the excess electrons are shared by more than one lattice Ti). The latter on the contrary tend to be localised surface species. Their optical absorption lies across the boundary visible/infra-red, thus generating the typical blue colour often associated with Ti^{3+} in TiO_2 when kept under O_2-deficient atmosphere. Lim et al.[8] lately studied the photocatalytic activity of Nb and N codoped TiO_2. Together with an experimentally proven enhanced photonic efficiency under visible light irradiation when both dopants are present (compared to the cases of either Nb or N single doping), their computed density of states (DOS) predicted a significant amount of Ti^{3+} in the lattice, somehow suggesting an analogy with the Biedrzycki's case of solely Nb doping. In this study we use an interesting combination of spectroscopic methods to investigate the simultaneous effect of Nb and N in the anatase lattice and reveal the nature of the Ti^{3+} species predicted by Lim et al.'s calculations. We report of an n-type character enhancement of the codoped semiconductor oxide associated with delocalised Ti^{3+} species. Furthermore by analysing electron paramagnetic resonance spectra in the dark and under irradiation we are able to provide an explanation for the photo-generation of paramagnetic charge carriers and the resulting photochemistry under visible light irradiation.

Continuous-wave electron paramagnetic resonance spectroscopy (CW-EPR) can provide evidence of paramagnetic species associated with crystal defects, including dopants. The identification of such species helps us to understand fundamental phenomena like charge compensation associated with aliovalent substitution of atoms/ions in lattice positions as well as the identification of interstitial species[9,10]. The analysis of optical properties such as valence to conduction band energy gaps can then be coupled with EPR spectroscopy to investigate the formation of charge carriers upon photon absorption. By comparing EPR spectra in the dark and under in-situ irradiation with ultra band gap photons, excitons (i.e. electron-hole pairs) dynamics, including formation and trapping, can be followed. Here, we focus on such an association between optical properties and paramagnetic species to assemble a puzzle of dynamics, function, and structural location of anatase dopants.

Figure 1 shows an X-ray diffraction pattern of a (Nb,N)-codoped TiO_2 oxide containing 0.1 at.% of Nb together with the pattern of a pure anatase; no crystalline phases other than

[a] *Danish Technological Institute, Gregersensvej 4, Taastrup, Denmark. Tel: +45 7220 2557; E-mail: anfl@teknologisk.dk*
[b] *Department of Chemistry, University of Aberdeen, Meston Building, Meston Walk. Aberdeen, UK. E-mail: a.folli@abdn.ac.uk.*

anatase are detectable in the doped sample. Diffuse relectance UV-vis spectra of the N- and Nb-codoped samples (Figure 2) are typical of anatase but with an additional feature emphasised in the Tauc plots (inset in Figure 2) for the codoped samples, corresponding to an energy gap (extrinsic band gap) of 2.29 eV ± 0.01 eV and likely to be associated with an electronic transition from an intra-band-gap state due to the presence of N doping [9,10] to the conduction band. This transition is responsible for the observed pale yellow colour of the material. The measured intrinsic and extrinsic absorption edges are not corrected for the phonon energy involved with the indirect transition and for the exciton binding energy. However, in the case of TiO_2 these quantities are on the order of thousandths of an electron-volt [11]. They are smaller than the average error on the measurement being on the order of hundredths of an electron-volt, and can therefore be neglected.

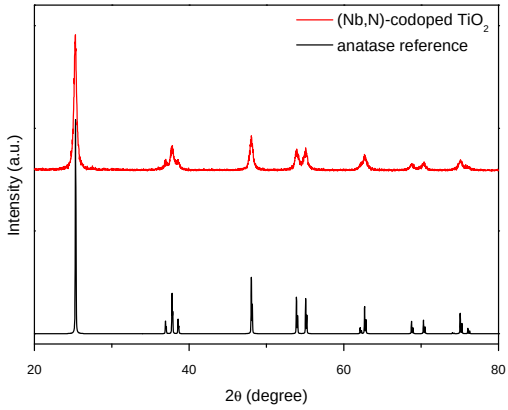

Fig. 1 XRD patterns for the (Nb,N)-codoped TiO_2 and anatase TiO_2 as a reference.

The conduction band edge was derived using electrochemical impedance spectroscopy (EIS) measurements as described elsewhere [12]. A Mott-Schottky plot was then constructed as reported in Figure 3 by plotting the inversed square of the space charge layer capacitance normalised for the contact area against the potential at which the C_{sc} was derived. The extrapolation of the linear trend in the Mott-Schottky plot to the x-axis (potential) led to the quantity $(U_{fb} + \frac{k_B T}{e})$ (see eq. 1) from which the flat band potential (U_{fb}, also representing the Fermi level since there is no band bending at flat band conditions) for a given semiconductor oxide could be derived. [13–15]

$$(C_{sc})^{-2} = \frac{2}{\varepsilon \cdot \varepsilon_0 \cdot e \cdot n_d} \cdot (U - U_{fb} - \frac{k_B T}{e}) \qquad (1)$$

Additionally, the donor density n_d was calculated from the slope of the linear part using a value of 41 for the dielectric constant of anatase. [16] As the donor density was found to be

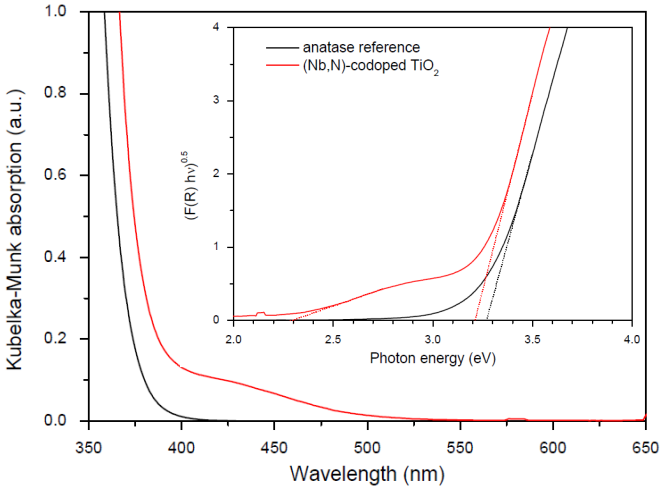

Fig. 2 Optical absorption spectra for the (Nb,N)-codoped TiO_2 and anatase TiO_2 as a reference. Inset: Tauc plots used to derive band gap values for the (Nb,N)-codoped TiO_2 and anatase TiO_2.

higher ($\geq 1 \times 10^{20}\,cm^{-3}$) than the effective density of states in the conduction band ($2.42 \times 10^{19}\,cm^{-3}$ assuming a value of $1.0\,m_e$ for the electron effective mass [17,18]), the energy difference between Fermi level and conduction band edge is very small ($< \frac{k_B T}{e} \approx 25\,mV$) and they can be assumed to be approximately the same ($U_{cb} \approx U_{fb}$) and equal to −0.2 V vs RHE, defining the positions of the valence band edge and intra-band-gap edge at +3.0 V and +2.1 V respectively. A schematic diagram of the band structure is given in Figure 4.

The specific nature of the dopants and visible-light active species could be deduced using EPR. Figure 5 shows the X-band (9.5 GHz) spectra of the (Nb,N)-codoped TiO_2 oxide in the dark and under in situ visible light irradiation (550 nm). Upon illumination, the EPR signal is modified compared with that from the non-illuminated sample. The experimental spectra are presented in Figure 5 together with the simulated spectra obtained using the SIM 32 simulation software. The very good agreement between fitted and experimental profiles allows the extraction of the characteristic EPR parameters as well as the precise description of each individual paramagnetic centre contributing to the overall spectrum. The nature of the EPR signals recorded can be described on the basis of three different EPR active centres for which $\boldsymbol{g}$ and $\boldsymbol{A}$ tensors are reported in Table 1. $\boldsymbol{g}$ and $\boldsymbol{A}$ tensors are also graphically visualised in Figure 5. The paramagnetic centre b1 can be attributed to adsorbed molecular $NO^{\cdot}$ [19,20] often detected in the cavities of sol-gel N-TiO_2 [20]. This species exhibits an anisotropic $\boldsymbol{g}$ tensor with rhombic symmetry, $g_{xx} \neq g_{yy} \neq g_{zz}$. The coupling of the unpaired electron with $^{14}_{7}N$ (nuclear spin $I = 1$; signal multiplicity $2I + 1 = 3$) develops a hyperfine structure characterized by 3 x 3 lines. The values reported

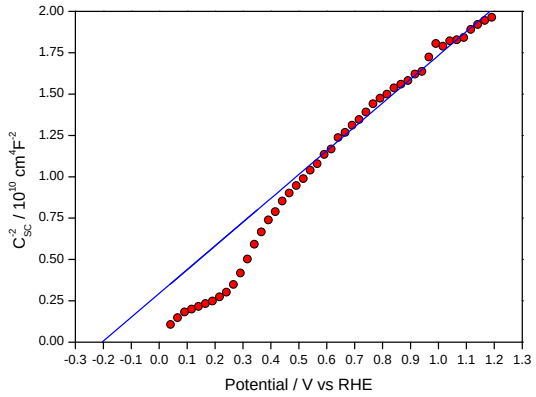

Fig. 3 Mott-Schottky plot of the electrode coated with the Nb, N codoped anatase TiO_2. The individual data points (red circles) were extrapolated to the x-axis by using linear regression (blue line). The regression did not take into account the points at lower potentials. In this region the inverse of the charge layer capacitance ($\frac{1}{C_{SC}}$) is low enough to be comparable with the inverse of the Helmholtz layer capacitance ($\frac{1}{C_H}$). The latter is therefore no longer negligible causing a deviation from the linear model.

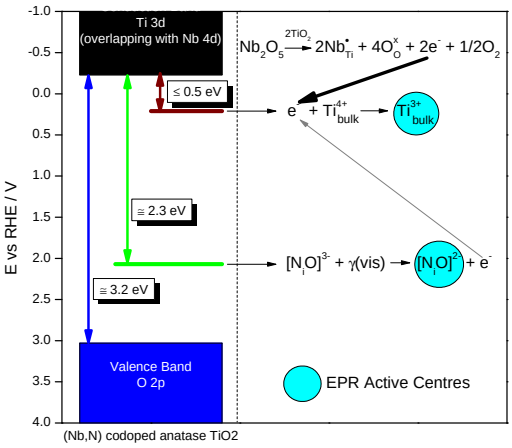

Fig. 4 Band structure diagram and paramagnetic species formation for (Nb,N) codoped TiO_2 containing 0.1 at.% of Nb.

in Table 1 are in good agreement with those reported elsewhere[9,19,20]. The paramagnetic center b2 consists of an interstitial N chemically bound to a lattice O ion forming a $N_iO^{\cdot}$ group carrying one electron in the singly occupied molecular orbital (SOMO). $N_iO^{\cdot}$ is effectively an intraband gap NO^{2-} state also exhibiting an anisotropic $\boldsymbol{g}$ tensor with rhombic symmetry, $g_{xx} \neq g_{yy} \neq g_{zz}$ (Table 1)[9,19,20]. As to its hyperfine structure, the electron in the SOMO couples with the non-zero spin $^{14}_{7}$N nucleus forming another set of 3 x 3 lines. b2's $\boldsymbol{g}$ tensor components were found to be shifted by 0.002 compared to previously reported values[9,10,19,21]. This shift may be associated with the influence of the transition metal dopant[9,21].

Nb occurs naturally as a single isotope, $^{93}_{41}$Nb, with 100 % abundance and nuclear spin $I = \frac{9}{2}$ (expected line multiplicity $2I+1 = 10$). Despite the high isotopic abundance of this high spin state nuclide, no super-hyperfine coupling (no signal splitting) between the single electron of the $N_iO^{\cdot}$ and the Nb nucleus was detected. This may be attributable to line broadening due to the use of powdered samples and the use of X band radiation, i.e. spectra were recorded at 9.5 GHz. It is likely that a well resolved 10 line super-hyperfine structure will be observable using single crystals and at 34 GHz (Q band)[22].

The paramagnetic center b3 consists of an axial $\boldsymbol{g}$ tensor having $g_{\perp} \neq g_{\parallel}$. The values reported in Table 1 of 1.988 and 1.957 are consistent with a signal attributable to Ti^{3+}. Although these values could be assigned to substitutional Ti^{3+} as reported by Kiwi at al.[23] and De Trizio et al.[4], they also match the values for interstitial Ti^{3+} found in colloidal TiO_2 by Howe and Grätzel[24]. The shape of the signal however seems to confirm substitutional bulk Ti^{3+} as observed in Nb-doped or F- and Nb-codoped anatase by Biedrzycki et al.[7]. The presence of Ti^{3+} can be explained by ion substitution and charge compensation. When Nb^{5+} replaces Ti^{4+} in the TiO_2 lattice, the excess positive charge must be compensated by an excess of negative charge, for example through an electronic compensation:

$$Nb_2O_5 \xrightarrow{2TiO_2} 2Nb_{Ti}^{\bullet} + 4O_O^x + 2e' + \frac{1}{2}O_2 \qquad (2)$$

In our codoped system another mechanism may also occur, where the charge compensation is provided by the other dopant, i.e. nitrogen species:

$$Nb_2O_5 + O_2 + 2NH_3 \xrightarrow{2TiO_2} 2Nb_{Ti}^{\bullet} + 2[NO]_O' + 2O_O^x + 3H_2O \qquad (3)$$

As far as the above charge compensation equations are concerned, all the species involved are diamagnetic apart from the free electrons generated through electronic compensation in Equation 2, that can indeed be trapped as Ti^{3+} ($Ti_{Ti}^{'}$) and/or Nb^{4+} (Nb_{Ti}^{x}) (d^1 paramagnetic metal cations, hence EPR active):

$$Ti_{Ti}^{x} + e' \longrightarrow Ti_{Ti}^{'} \qquad (4)$$

$$Nb_{Ti}^{\bullet} + e' \longrightarrow Nb_{Ti}^{x} \qquad (5)$$

We did not observe Nb^{4+} at 77 K (and above), however this could be due to its signal broadening beyond detection at this

Table 1 Spin Hamiltonian parameters (***g*** and ***A*** tensors) for the 3 active EPR centres detected in (Nb,N) codoped TiO_2 at 77 K and 9.5 GHz, including line width and relative contribution. The values in brackets refer to the best fit under visible light irradiation

EPR Centre	Paramagnetic species	g_{xx}	g_{yy}	g_{zz}	A_{xx} G	A_{yy} G	A_{zz} G	W_{xx} G	W_{yy} G	W_{zz} G	Relative Contribution %
b1	adsorbed $NO^{\cdot}$	2.001	1.996	1.927	< 1	31.4	10.1	9(10)	9(10)	9(10)	14.3(6.4)
b2	NO^{2-}	2.003	2.002	2.001	2.3	4.4	32.3	6(7)	6(7)	6(7)	14.3(55.3)
b3	Ti^{3+}	1.988	1.957	-	-	-	-	5	5	5	71.4(38.3)

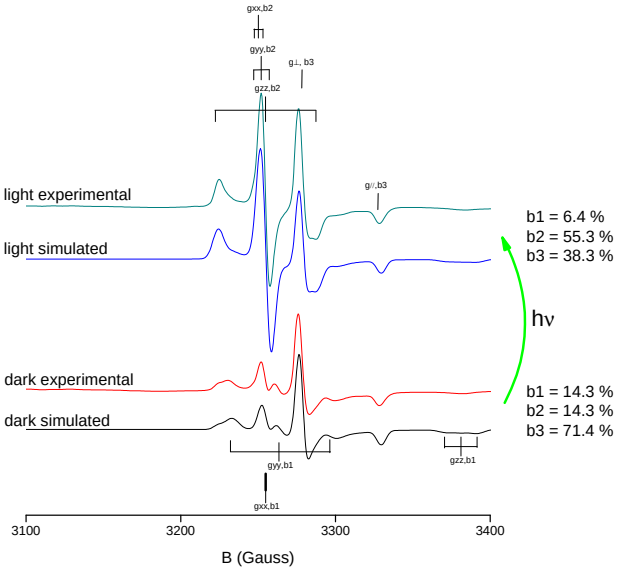

Fig. 5 EPR spectra at 77 K in the dark and under in situ irradiation with 550 nm wavelength visible light for (Nb,N)-codoped TiO_2.

temperature[23]. Nb^{4+} is characterised by a very short spin relaxation time[22,25] and it was observed in Nb-doped rutile single crystals[22,25] and in Nb-doped TiO_2 powders containing both anatase and rutile[23] at 4.2 K only. However De Trizio et al.[4] at the same temperature could not detect Nb^{4+} in Nb-doped colloidal anatase nanocrystals. A further investigation (not reported here) was conducted using EPR spectroscopy at 4.2 K to confirm potential presence of Nb^{4+} in our (Nb,N)-codoped systems. In line with De Trizio et al.'s findings[4], we could not observe any Nb^{4+} in our codoped anatase samples. These results seem to suggest that the energetics or the kinetics of reaction 5 could significantly vary between anatase and rutile polymorphs. It is important to mention that a third mechanism is also possible, i.e. ionic compensation through Ti vacancies:

$$2\,Nb_2O_5 \xrightarrow{5\,TiO_2} 4\,Nb_{Ti}^{\bullet} + V_{Ti}^{////} + 10\,O_O^{x} \qquad (6)$$

The experimental detection of Ti vacancies is a challenging task and on the basis of our experimental observations we are not able to quantify the real contribution of such a compensation mechanism. However, as already highlighted by Biedrzycki et al.[7], aliovalently doped systems seem to selectively favour the solution of higher stability, hence the extensive presence of Ti^{3+} ions would indicate much higher contribution of the mechanism of valence induction over that one of vacancy formation. The bulk substitutional Ti^{3+} ions created by such a valence induction tend to have the unpaired electron delocalised beyond the first coordination sphere, which would explain the high conductivity typical of these doped oxides[7,26].

The visible light photo-induced electron injection is mainly driven by the discrete N donor levels situated in the band gap, Figure 4. This can be proven by comparing the EPR spectra in the dark and under visible light (550 nm) illumination. A large fraction of the nitrogen centres is diamagnetic before light irradiation, carrying two paired electrons in the highest occupied molecular orbital (HOMO), designated N_iO^{-}, i.e. intraband gap NO^{3-} states. Upon irradiation with visible light, electron transitions CB $\leftarrow$ NO^{3-} occur, leaving behind a much larger quantity of paramagnetic NO^{2-} states. As we already proved for (W,N)-codoped TiO_2[9], this mechanism is confirmed by the fact that by increasing the relative contribution of the b2 species in the simulation from 14.3 % to 55.3 % (accordingly the b1 and b3 signal contributions drop from 14.3 % and 71.4 % to 6.4 % and 38.3 % respectively), the simulated dark spectrum turns into a new profile which perfectly matches the spectrum recorded under in-situ visible light irradiation, Figure 5. Interestingly, although the relative contribution of the b3 centre decreases (b2 signal very intense), its absolute intensity actually increases. This seem

to suggest that the photo-injected electrons can be trapped to form exactly the same type of reduced Ti^{3+} centres already present in the initial material.

In conclusion, doping anatase TiO_2 with both Nb and N demonstrated to improve optical and electronic properties. EPR experimentally proved a valence-induced n-type character enhancement that can be explained through shallow trapping of charge compensation electrons and formation of bulk substitutional Ti^{3+} species. The presence of these species is associated with an increased conductivity and improved O_2 affinity exhibited by Nb-containing titanias compared to the case of pure, undoped TiO_2. In addition, the formation of electron-hole pairs sensitised by visible light is a consequence of electron transitions from the HOMO of NO^{3-} species ($[NO]_O^{\cdot}$ in Kröger-Vink notation) to the conduction band. The electrons photo-injected in the conduction band can be trapped as bulk substitutional Ti^{3+} species too, as confirmed by the increased absolute intensity of the b3 EPR signal under in-situ visible light irradiation and absence of any other known Ti^{3+} species signals. Using a different approach for the electron injection (photo-injection rather than chemical reduction like in Biedrzycki et al.[7]), we corroborate the theory that the high conductivity of the starting material induces the formation of more of the same bulk reduced centres (responsible for the high conductivity in the first place), when extra electrons are injected. This seems to be very different from the case of pure undoped anatase TiO_2 where electron injection generates very localised surface Ti^{3+} species.

1 Acknowledgements

We thank the European Commission for the financial support through the European Project Light2CAT. Light2CAT is funded by the European Unions Seventh Framework Programme (FP7) under the grant agreement no. 283062 Eco-Innovation, Theme Environment.

References

1 F. A. Grant, *Rev. Mod. Phys.*, 1959, **31**, 646–674.
2 S. Lee, J. H. Noh, H. S. Han, D. K. Yim, D. H. Kim, J.-k. Lee, J. Y. Kim, H. S. Jung and K. S. Hong, *J. Phys. Chem. C*, 2009, **113**, 6878–6882.
3 T. Hitosugi, N. Yamada, S. Nakao, Y. Hirose and T. Hasegawa, *Phys. Status Solidi (a)*, 2010, **207**, 1529–1537.
4 L. De Trizio, R. Buonsanti, A. M. Schimpf, A. Llordes, D. R. Gamelin, R. Simonutti and D. J. Milliron, *Chemistry of Materials*, 2013, **25**, 3383–3390.
5 J. Kasai, T. Hitosugi, M. Moriyama, K. Goshonoo, N. L. H. Hoang, S. Nakao, N. Yamada and T. Hasegawa, *J. App. Phys.*, 2010, **107**, 053110.
6 C. Tasaki, N. Oka, T. Yagi, N. Taketoshi, T. Baba, T. Kamiyama, S.-i. Nakamura and Y. Shigesato, *Jpn. J. App. Phys.*, 2012, **51**, 035802.
7 J. Biedrzycki, S. Livraghi, E. Giamello, S. Agnoli and G. Granozzi, *J. Phys. Chem. C*, 2014, **118**, 8462–8473.
8 J. Lim, P. Murugan, N. Lakshminarasimhan, J. Y. Kim, J. S. Lee, S.-H. Lee and W. Choi, *J. Catal.*, 2014, **310**, 91–99.
9 A. Folli, J. Z. Bloh, E.-p. Beukes, R. F. Howe and D. E. Macphee, *J. Phys. Chem. C*, 2013, **117**, 22149–22155.
10 G. Barolo, S. Livraghi, M. Chiesa, M. C. Paganini and E. Giamello, *J. Phys. Chem. C*, 2012, **116**, 20887–20894.
11 J. Pascual, J. Camassel and H. Mathieu, *Phys. Rev. B*, 1978, **18**, 5606–5614.
12 J. Z. Bloh, A. Folli and D. E. Macphee, *J. Phys. Chem. C*, 2014, **118**, 21281–21292.
13 N. F. Mott, *P. Roy. Soc. Lond. A Mat.*, 1939, **171**, 27–38.
14 W. Schottky, *Z. Phys.*, 1939, **113**, 367–414.
15 W. Schottky, *Z. Phys.*, 1942, **118**, 539–592.
16 I. Oja, A. Mere, M. Krunks, R. Nisumaa, C.-H. Solterbeck and M. Es-Souni, *Thin Solid Films*, 2006, **515**, 674–677.
17 H. Tang, K. Prasad, R. Sanjines, P. E. Schmid and F. Levy, *J. Appl. Phys.*, 1994, **75**, 2042.
18 B. Enright and D. Fitzmaurice, *J. Phys. Chem.*, 1996, **100**, 1027–1035.
19 C. Di Valentin, E. Finazzi, G. Pacchioni, A. Selloni, S. Livraghi, M. C. Paganini and E. Giamello, *Chem. Phys.*, 2007, **339**, 44–56.
20 S. Livraghi, M. R. Chierotti, E. Giamello, G. Magnacca, M. C. Paganini, G. Cappelletti and C. L. Bianchi, *J. Phys. Chem. C*, 2008, **112**, 17244–17252.
21 A. M. Czoska, S. Livraghi, M. C. Paganini, E. Giamello, C. Di Valentin and G. Pacchioni, *Phys. Chem. Chem. Phys.*, 2011, **13**, 136–143.
22 P. H. Zimmermann, *Phys. Rev. B*, 1973, **8**, 3917–3927.
23 J. Kiwi, J. T. Suss and S. Szapiro, *Chem. Phys. Lett.*, 1984, **106**, 3–6.
24 R. F. Howe and M. Gratzel, *J. Phys. Chem.*, 1985, **89**, 4495–4499.
25 P. F. Chester, *J. App. Phys.*, 1961, **32**, 866.
26 S. Livraghi, M. Chiesa, M. C. Paganini and E. Giamello, *J. Phys. Chem. C*, 2011, **115**, 25413–25421.